Journal of Nonlinear and Convex Analysis
Volume 26, Number 7, 2025, 2357–2374

Yokohama Publishers
ISSN 1880-5221 ONLINE JOURNAL

A DISTRIBUTED ADAPTIVE CONTROL STRATEGY FOR MICROGRIDS CONSIDERING POWER FLOW CONSTRAINTS

ZHUOHUAN LI, DUOTONG YANG*, CHANGCHENG ZHOU, KAI CHENG, YANG YU, AND SIRUI YANG

Abstract. This paper presents a distributed adaptive control algorithm for microgrid voltage-frequency synchronization and active power allocation regulation. The algorithm significantly reduces the dependence on traditional local information measurement by introducing global information and distributed coordination mechanisms, thereby improving control efficiency and stability. The algorithm uses an improved distributed consensus method to achieve fast synchronization of voltage and frequency and allows real-time adjustment of the output of each distributed generation unit to ensure that frequency and voltage deviations remain within a minimum range, achieving stable operation. For active power allocation, the algorithm can adaptively adjust power output to achieve proportional allocation, effectively managing load changes and output fluctuations. Real-time simulation verification shows that the proposed adaptive distributed control algorithm performs well in voltage-frequency synchronization and active power allocation, providing reliable support for the efficient and stable operation of microgrids.

1. Introduction

With the rising energy demand and worsening environmental pollution, Distributed Generation (DG) technology based on renewable energy has rapidly developed and been widely applied. Microgrids, as a flexible and reliable means of integrating renewable energy into the main grid, have become a research focus. They can operate in grid-connected mode or independently in island mode. Particularly in island mode, microgrids must maintain system voltage and frequency stability without main grid support while achieving economically efficient power distribution [8, 10, 12, 13].

Control strategies are crucial for microgrid stability. Traditional droop control often struggles with power allocation due to line impedance, leading to voltage and frequency deviations. To address this, improved methods like hierarchical control, virtual synchronous generator control, and model predictive control have been proposed. These strategies enhance local and secondary control layers, achieving precise voltage, frequency, and power control while improving stability and robustness [3, 11, 15, 19, 20, 22].

2020 *Mathematics Subject Classification.* 93C40.

Key words and phrases. Microgrid, distributed adaptive control, power flow constraints, voltage/frequency control.

China Southern Power Grid DigitalGrid Research Institute Co., Ltd, Self-fundedInnovation Project(670000KK52220003).

*Corresponding author.

Distributed control and optimization scheduling are also key research areas. Techniques like event-triggered control, distributed consensus algorithms, and delay-tolerant strategies reduce system errors and enhance control system efficiency. These approaches have been theoretically validated and applied in practical scenarios, laying a foundation for the large-scale adoption of microgrids [2, 4, 5, 7, 9, 14, 18].

Power balance constraints are critical for microgrid stability [21]. Frequency fluctuations, influenced by internal generators and loads, must be controlled to stay within defined ranges, typically 0.2 Hz. For instance, a frequency-constrained energy management system [1] addresses short-term power fluctuations, improving regulation performance. Similarly, consensus algorithms [6] adjust DG outputs to optimize economic performance while meeting capacity constraints. Power balance is further maintained through load scheduling and equipment control [16, 17, 23], improving robustness and efficiency.

This paper proposes an adaptive distributed control algorithm for frequency synchronization and active power distribution adjustment. Unlike traditional methods that heavily rely on local information, the proposed algorithm introduces global information and distributed coordination, simplifying measurement and communication while enhancing robustness. It achieves voltage and frequency synchronization within a limited time, improving active power flow constraints and overall microgrid stability.

The algorithm also adaptively adjusts power output for proportional distribution, responding effectively to load changes and generation fluctuations while maintaining high distribution accuracy across different modes. It employs an enhanced distributed consensus method, ensuring voltage-frequency synchronization, real-time output adjustments, and minimal deviations. The cooperative control design aligns DG frequencies with reference values while meeting power flow constraints, enabling precise voltage, frequency, and power control and enhancing system stability c1.

In summary, the proposed adaptive distributed control algorithm advances voltage-frequency synchronization and active power distribution regulation, reducing reliance on local measurements, improving stability, and offering reliable support for efficient microgrid operation.

2. Methodology

The secondary control of a microgrid is a synchronization tracking problem, where all DGs attempt to synchronize their terminal voltage magnitudes and frequencies to predefined reference values. In the synchronization tracking problem, all individual agents seek to synchronize with a leader that generates the command. To achieve this functionality, each DG needs to communicate with neighboring DGs and receive information from them. The required communication network can be modeled using a directed communication graph.

For the physical network of an AC microgrid, let $\mathcal{G}_{\mathrm{p}}(\mathcal{V}, \mathcal{E}, \mathcal{A})$ represent a simple undirected graph without self-loops, where $\mathcal{V} = \{\mathcal{V}_0, \ldots, \mathcal{V}_{n-1}\}$ is the set of DG nodes, $\mathcal{E} \subseteq \mathcal{V} \times \mathcal{V}$ is the set of physical links, and $\mathcal{A} \in \mathbb{R}^{n \times n}$ is the adjacency matrix. The elements of $\mathcal{A}$ satisfy that for each undirected edge $e = (\mathcal{V}_i, \mathcal{V}_j) \in \mathcal{E}$, $a_{ij} > 0$, otherwise $a_{ij} = 0$. For each node $i \in \mathcal{V}$, the degree is defined as $d_i = \sum a_{ij}$, and the corresponding degree matrix is D. The incidence matrix of $\mathcal{G}$, denoted as

$\mathcal{B} = [b_{ie}] \in \mathbb{R}^{n\times|\mathcal{E}|}$, is defined as follows: if vertex i and edge e are not incident, then $b_{ie} = 0$; otherwise, if edge e originates from vertex i, then $b_{ie} = -1$, and if e terminates at vertex i, then $b_{ie} = 1$. If the graph $\mathcal{G}_{\mathrm{p}}(\mathcal{V}, \mathcal{E}, \mathcal{A})$ is connected, then the rank of $\mathcal{B}$ is $\mathrm{rank}(\mathcal{B}) = n - 1$. The weighted symmetric Laplacian matrix is $\mathcal{L} = \mathcal{B}W\mathcal{B}^{\top}$, where $W = \mathrm{diag}\big(\{a_{ij}\}_{\{ij\}\in\mathcal{E}}\big) \in \mathbb{R}^{|\mathcal{E}|\times|\mathcal{E}|}$. The set of neighbors of DG_i is denoted as $\mathcal{N}_i = \{\mathcal{V}_j | (\mathcal{V}_i, \mathcal{V}_j) \in \mathcal{E}\}$.

Lemma 2.1. *If the directed graph G has a directed spanning tree and at least one root node $g_i \neq 0$, then*

$$\|\delta\| \leq \|e\| / \sigma(L + G)_{\min}$$

where $\sigma(L + G)_{\min}$ is the smallest singular value of $L + G$, and $e = 0$ if and only if all nodes are synchronized.

Lemma 2.2. *If the directed graph G has a spanning tree and at least one root node $g_i \neq 0$, let $P = \mathrm{diag}\{1/w_i\}$, where w_i are the elements of the vector W, and W satisfies $AW = 1_N$, with $A \equiv L + G$. Then, $Q \equiv PA + A^T P$ is positive definite.*

First, consider an AC microgrid operating in island mode, with its physical network topology denoted as $\mathcal{G}_{\mathrm{p}}$. Through DC/AC inverters with frequency droop controllers, all distributed generators (DGs) supply the load and inject active power into the network. The DG nodes are represented by the subset $\mathcal{V}_D \subset \mathcal{V}$. The set $\mathcal{L} := \mathcal{V}\backslash\mathcal{V}_D$ represents the load nodes. Label all nodes in order such that $\mathcal{L} := \mathcal{V}\backslash\mathcal{V}_D$, and $\mathcal{V}_L = m + 1, \ldots, n$. According to the droop control principle, the dynamics of the microgrid can be expressed by the following swing equations:

$$\begin{aligned} \dot{\theta}_i &= \delta\omega_{ni} - m_{Pi} \sum_{\mathcal{V}_i\in\mathcal{N}_i} E_i E_j |Y_{ij}| \sin(\theta_i - \theta_j), \ \mathcal{V}_i \in \mathcal{V}_D, \\ \dot{\theta}_i &= -m_{Pi} P_{L,i} - m_i^P \sum_{\mathcal{V}_i\in\mathcal{N}_i} E_i E_j |Y_{ij}| \sin(\theta_i - \theta_j), \ \mathcal{V}_i \in \mathcal{V}_L. \end{aligned} \tag{2.1}$$

Here, when $\mathcal{V}_i \in \mathcal{V}_L$, ${P_i}^L > 0$ is the power demand of the load, and $m_i^P > 0$ is the frequency-dependent parameter. If the load is independent of frequency, then $m_i^P \to 0$. According to Kirchhoff's Current Law (KCL), the actual power flow from node $\mathcal{V}_i$ to $\mathcal{V}_j$ is $V_i V_j |Y_{ij}| \sin(\theta_i - \theta_j)$. θ_i is the voltage phase angle, and Y_{ij} is the admittance of the physical connection between nodes $\mathcal{V}_i$ and $\mathcal{V}_j$. $\delta\omega_i = \dot{\theta}_i = \omega_i - \omega_{\mathrm{ref}}$ is the deviation of the frequency at DG_i from the nominal frequency, which can be $2\pi \cdot 50$ or $2\pi \cdot 60$Hz, while ${\delta\omega_i}^{\mathrm{nom}} = \omega_{ni} - \omega_{\mathrm{ref}}$.

Additionally, $P_i = \sum_{\mathcal{V}_i\in\mathcal{N}i} E_i E_j |Y_{ij}| \sin(\theta_i - \theta_j)$ is the active power injected into or absorbed by the power network at node $\mathcal{V}_i$. For simplification, the coupling strength of different physical connections $e = (\mathcal{V}_i, \mathcal{V}_j) \in \mathcal{E}$ is represented as $K_{ij} = V_i V_j |Y_{ij}| \in \mathbb{R}$. If a synchronous solution exists for system (1), then there exists $\omega_{\mathrm{syn}} \in \mathbb{R}$ such that, for $i \in \mathcal{V}$, $\omega_{\mathrm{syn}} = \lim_{t\to\infty} \dot{\theta}_i(t) = \lim_{k\to\infty} \delta\omega_i(t)$, and there exist $\gamma \in [0, \pi/2)$ and $\omega_{\mathrm{syn}} \in \mathbb{R}$ such that let $\lim_{t\to\infty} \theta(t) \in \bar{\Delta}_G(\gamma)$. among $\bar{\Delta}_G(\gamma) = \{(\theta_1, \ldots \theta_n) : |\theta_i - \theta_j| \leq \gamma, \forall\{i, j\} \in \mathcal{E}\}$, and $\lim_{t\to\infty} \dot{\theta}(t) = \omega_{\mathrm{syn}} 1_n$. This is obtained by summing all equations in (2.1).

$$\omega_{\mathrm{syn}} = lim_{t\to\infty} \frac{\sum_{\mathcal{V}_i\in\mathcal{V}} D\delta\omega_{ni}/m_{Pi} - \sum_{\mathcal{V}_i\in\mathcal{V}_L} P_{L,i}}{\sum_{\mathcal{V}_i\in\mathcal{V}} \frac{1}{m_i}}.$$

In fact, ω_{syn} represents the global frequency deviation of the network from the nominal frequency ω^{rated} under frequency synchronization.

The power flow on each physical link is constrained by the power flow equations, so the desired value of the frequency cannot be arbitrarily chosen. Next, we will analyze the design of frequency expectations $\delta\omega_{ni}$ considering the power flow constraints.

Let $\delta\omega \triangleq [\delta\omega_1, \ldots, \delta\omega_n]^T$, $\delta\hat{\omega} \triangleq [\delta\omega_1, \ldots, \delta\omega_m]^T$, $\delta\omega^{\text{nom}} \triangleq [\delta\omega_1^{\text{nom}}, \ldots, \delta\omega_m^{\text{nom}}]^T$, $\theta \triangleq [\theta_1, \ldots, \theta_n]^T$, $P \triangleq [P_1, \ldots, P_n]^T$, $\mathcal{M}_P = \text{diag}\left(\left\{m_i^P\right\}_{\mathcal{V}_i \in \mathcal{V}}\right) \in \mathbb{R}^{n\times n}$, $\widehat{\mathcal{M}_P} = \text{diag}\left(\left\{m_i^P\right\}_{\mathcal{V}_i \in \mathcal{V}_D}\right) \in \mathbb{R}^{m\times m}$, $\mathcal{M}_P = \text{diag}\left(\left\{m_i^P\right\}_{\mathcal{V}_i \in \mathcal{V}_L}\right) \in \mathbb{R}^{(n-m)\times(n-m)}$ and $W = \text{diag}\left(\left\{K_e\right\}_{(\mathcal{V}_i,\mathcal{V}_j)\in\mathcal{E}}\right) \in \mathbb{R}^{|\mathcal{E}|\times|\mathcal{E}|}$. According to the swing equation of the microgrid, there is a deformation formula:

$$P^{\text{set}}(t) - \mathcal{M}_P^{-1}\delta\omega(t) = \mathcal{B}W\sin\left(\mathcal{B}^T\theta(t)\right)$$

record $P^{\text{set}}(t) - \mathcal{M}_P^{-1}\delta\omega(t) = \underline{\mathcal{P}}(t)$, have

$$\underline{\mathcal{P}}(t) = \mathcal{B}W\sin\left(\mathcal{B}^T\theta(t)\right). \tag{2.2}$$

Next, the conditions for the existence of synchronous solutions to the power flow equation (2.2) are analyzed. make $\psi \triangleq \sin\left(\mathcal{B}^\top\theta\right) \in \mathbb{R}^{|\mathcal{E}|}$. Equilibrium point θ satisfy:

$$\underline{\mathcal{P}} = \mathcal{B}W\psi. \tag{2.3}$$

Note that according to the definition of the Moore-Penrose pseudoinverse, $\left(I_n - \mathcal{B}\mathcal{B}^\dagger\right)\mathcal{B} = \mathbf{0}_{|\mathcal{E}|}$. Therefore, each row of $I_n - \mathcal{B}\mathcal{B}^\dagger$ lies in the left null space of $\mathcal{B}$, which is spanned by ${\mathbf{1}_n}^T$. Since $I_n - \mathcal{B}\mathcal{B}^\dagger$ is symmetric, it follows that all its elements are identical. And since $\underline{\mathcal{P}} \in {\mathbf{1}_n}^\perp$, it is clear that $\left(I_n - \mathcal{B}WW^{-1}\mathcal{B}^\dagger\right)\underline{\mathcal{P}} = \mathbf{0}_n$, which means that $W^{-1}\mathcal{B}^\dagger\underline{\mathcal{P}}$ is a particular solution of (2.2). Therefore, the solution of equation (2.2) takes the form:

$$\psi = W^{-1}\mathcal{B}^\dagger\underline{\mathcal{P}} + \psi_h \tag{2.4}$$

where $\psi_h \in \ker(\mathcal{B})$ is the homogeneous solution. Furthermore, it can be written as:

$$\sin\left(B^\top\theta\right) = W^{-1}B^\dagger\underline{\mathcal{P}} + \psi_h. \tag{2.5}$$

Due to the existence of the last term in equation (2.5), unless $\mathcal{G}$ is an acyclic graph (where $\ker(\mathcal{B}) = \emptyset$ for acyclic graphs), it is difficult to establish a relationship between $\sin\left(\mathcal{B}^T\theta\right)$ and $W^{-1}\mathcal{B}^\dagger\underline{\mathcal{P}}$. It is noted that the following sufficient synchronization condition ensures the existence of a locally exponentially stable frequency synchronization solution $\theta^* \in \Delta_G(\gamma), \gamma \in [0, \pi/2)$ for model (2.2):

$$\left\|\mathcal{L}^\dagger\underline{\mathcal{P}}\right\|_{\mathcal{E},\infty} = \left\|\mathcal{B}^T\mathcal{L}^\dagger\underline{\mathcal{P}}\right\|_\infty \leq g\left(\left\|B^TL^\dagger BW\right\|\right) \tag{2.6}$$

where $g\left(\left|\mathcal{B}^\top\mathcal{L}^\dagger\mathcal{B}W\right|\right)$ is defined as:

$$g = \left(\frac{\gamma_\infty^* + \sin\left(\gamma_\infty^*\right)}{2}\right) - \left\|\mathcal{B}^\top\mathcal{L}^\dagger\mathcal{B}W\right\|_\infty\left(\frac{\gamma_\infty^* - \sin\left(\gamma_\infty^*\right)}{2}\right). \tag{2.7}$$

Among them, $\gamma_{\infty}^{*} = \arccos\left(\frac{|B^{\top}L^{\dagger}BW|_{\infty}-1}{|B^{\top}L^{\dagger}BW|_{\infty}+1}\right) \in \left[0, \frac{\pi}{2}\right)$. By making the substitution in condition (2.6) $(\mathcal{L})^{\dagger} \to W^{-1}\left(\mathcal{B}\mathcal{B}^{\top}\right)^{\dagger}$ and $\mathcal{B}^{\top}\left(\mathcal{B}\mathcal{B}^{\top}\right)^{\dagger} \to \mathcal{B}^{\dagger}$, can infer

$$\left\|W^{-1}\mathcal{B}^{\dagger}\underline{\mathcal{P}}\right\|_{\infty} \leq \mathrm{g}. \tag{2.8}$$

Then the sufficient condition of power flow balance can be deduced

$$\Phi = \left\{\mathcal{M}_P\underline{\mathcal{P}}(t) \in \mathbb{R}^n \mid \|\mathcal{M}_P\underline{\mathcal{P}}\|_{\infty} \leq \bar{\eta}\right\}. \tag{2.9}$$

3. Parameter adaptive frequency and active power distribution control design considering power flow balance constraints

Next, we will design a cooperative control algorithm to synchronize the frequency of all Distributed Generators (DGs) to a reference frequency ω_{ref} while ensuring that power flow constraints are satisfied during synchronization. Based on the analysis from the first part, secondary frequency control involves selecting appropriate inputs ω_{ni} to adapt to the previously proposed droop characteristics. Taking the derivative of the frequency droop characteristics, we get:

$$\dot{\omega}_i = \dot{\omega}_{ni} - m_{Pi}\dot{P} = u_{\omega i}. \tag{3.1}$$

Here $u_{\omega i}$ is an auxiliary control quantity. In this dynamic system, the control input ω_{ni} is obtained by calculating $u_{\omega i}$, and the control input ω_{ni} is obtained by calculating $u_{\omega I}$. So, the quadratic frequency control problem of a microgrid containing n DGS is transformed into a tracking synchronization problem of a first-order linear multi-agent system. Like voltage synchronization, in order to realize the synchronization of all DG frequencies, it is assumed that the DGS communicate with each other through a prescribed communication directed graph G. The auxiliary control quantity $u_{\omega i}$ is selected based on its own information and the information of its neighbors in the directed graph, which is described as follows.

$$\begin{aligned} u_{\omega i} &= -c_{\omega}e_{\omega i}; \\ e_{\omega i} &= \sum_{j\in N_i} a_{ij}\left(\omega_i - \omega_j\right) + g_i\left(\omega_i - \omega_{ref}\right). \end{aligned} \tag{3.2}$$

To show that the proposed controller can achieve synchronization for w_i, considering Lemmas 2.1 and 2.2, the global neighbor error vector above can be written as follows.

$$e = (L+G) \bullet (\omega - \omega_{\mathrm{ref}}) \equiv (L+G)\delta. \tag{3.3}$$

Where global variables $\omega = \begin{bmatrix} \omega_1 & \omega_2 & \dots & \omega_N \end{bmatrix}^T$, $e = \begin{bmatrix} e_{\omega 1} & e_{\omega 2} & \dots & e_{\omega N} \end{bmatrix}^T$, $v_{ref} = 1_N \otimes v_{ref}$, 1_N. It's a unit vector of length N. $\otimes$ represents the Kronecker product, $G \in \Re^{N\times N}$ is a diagonal matrix whose diagonal values are equal to g_i, and δ is a globally inconsistent vector.

This formulation obtains the global neighbor error vector by calculating the error between the terminal voltage amplitude and frequency of each DG and a predetermined reference value. This vector reflects the difference between each DG in the system and the global reference value, which is an important basis for subsequent synchronization control and power allocation adjustment.

The secondary frequency control input ω_{ni} based on distributed cooperative control is written as:

$$\omega_{ni} = \int (u_{\omega i} + m_{Pi}\dot{P}_i)dt. \tag{3.4}$$

The computation of the control input is the core part of the control algorithm. Through this formula, the global neighbor error vector can be transformed into specific control commands, so as to realize the synchronous control of the voltage and frequency of each DG and the adjustment of the power allocation.

It should be noted that once the frequency is controlled twice, the power between each DG must meet the power proportion output of the primary control, which satisfies the following equation:

$$m_{P1}P_1 = \cdots = m_{PN}P_N. \tag{3.5}$$

Therefore, to satisfy the frequency output, it is necessary to consider the distributed cooperative control of $m_{Pi}\dot{P}_i$, which is the regulator synchronization problem of linear first-order multi-agent systems. In order to realize synchronization, it is assumed that DG communicate with each other through the specified communication digraph G, and the auxiliary control quantity $m_{Pi}\dot{P}_i$ is selected based on its own information and the information of neighbors in the digraph, which is specifically described as:

$$u_{pi} = -e_{zi}. \tag{3.6}$$

Among

$$e_{pi} = \sum_{j\in N_i} \hat{a}_{1ij} \cos(\theta_i - \theta_j)(m_{Pi}P_i - m_{Pj}P_j),$$

$$\dot{\hat{a}}_{1ij} = \vartheta_{ij} a_{ij} \omega_i (\cos(\theta_i - \theta_j))(m_{Pi}P_i - m_{Pj}P_j).$$

The secondary frequency control block diagram based on distributed cooperative control is shown in Figure 1.

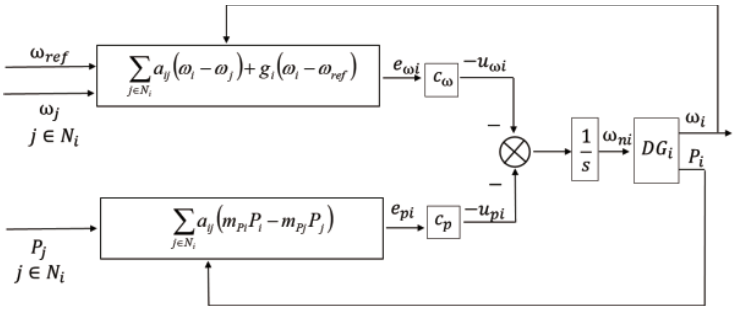

FIGURE 1. Block Diagram of Distributed Cooperative Secondary Frequency Control

As shown, the control input ω_{ni} can be rewritten as:

$$\omega_{ni} = \int (u_{\omega i} + u_{pi})dt. \tag{3.7}$$

Then the stability analysis of the above adaptive controller can be concluded as follows:

Theorem 3.1. *If the directed graph G has a spanning tree and at least one root node $g_i \neq 0$, then choosing the u_{vi} proposed above, the global neighbor error e is asymptotically stable. Moreover, the output frequency ω of the DG synchronizes with ω_{ref}, and the active power is allocated proportionally.*

Proof. The global input u_{vi} is given by: $u_\omega = \begin{bmatrix} u_{\omega 1} & u_{\omega 2} & \dots & u_{\omega N} \end{bmatrix}^T = -c_\omega e$.

Select the following Lyapunov function:

$$V = \frac{1}{2} e^T P e + y^T M^{-1} y + \sum_i \sum_j \frac{1}{\vartheta_{ij}} \tilde{a}_{1ij} \tilde{a}_{1j},\ P = P^T, P > 0 \tag{3.8}$$

where $\tilde{a}_{1ij} = \hat{a}_{1ij} - a_{1ij}$. Based on the above derivation, differentiate the Lyapunov function and define $v_{od} = u_v$ to get:

$$\begin{aligned} \dot{V} &= e^T P \dot{e} + \dot{y}^T M^{-1} y + \sum_i \sum_j \frac{1}{\vartheta_{ij}} \dot{\tilde{a}}_{1,j} \tilde{a}_{1ij} \\ &= e^T P (L+G)(\dot{\omega}) + \dot{y}^T M^{-1} y + \sum_i \sum_j \frac{1}{\vartheta_{ij}} \dot{\tilde{a}}_{1,j} \tilde{a}_{1jj} \\ &= e^T P (L+G)\left(u_\omega\right) - z^T \tilde{L}_1^T \omega + \sum_i \omega_i \tilde{L}_1 z \end{aligned} \tag{3.9}$$

where $y = \begin{bmatrix} m_{P1} P_1 & m_{P2} P_2 & \dots & m_{PN} P_N \end{bmatrix}^T$, $L_1 = H \mathrm{diag}\left\{\alpha_{1jj} \cos\left(\theta_i - \theta_j\right)\right\} H^T$, $\hat{L}1 = H \mathrm{diag}(\hat{a}1ij \cos\left(\theta_i - \theta_j\right) H^T$, $\tilde{L}_1 = \hat{L}_1 - L_1$. Considering $A \equiv L + G$, the above expression simplifies to:

$$\dot{V} = -c_\omega e^T P A e = \frac{-c_\omega}{2} e^T \left(PA + A^T P\right) e. \tag{3.10}$$

From Lemma 2.2, we know that the matrix $Q \equiv PA + A^T P$ is positive definite, so the term $\frac{-c_\omega}{2} e^T Q e$ is negative definite. Therefore, the global neighbor error e is asymptotically stable. From Lemma 2.1, we can see that the global inconsistency vector δ is asymptotically stable, and the DG output voltage direct term v_{odi} synchronizes with v_{ref}. The proof is complete. □

Next, we will prove that under the proposed two-layer control strategy, the power flow constraints will be perfectly satisfied. Let $\zeta(t) = \left[\delta\omega^T, \delta\omega_n^T\right]^T$, and to satisfy the constraint condition (2.9), we transform the problem into the following new problem: If the system consisting of the two-layer control (2.1), (3.2), and (3.6) can be represented by the state-space system matrix $\mathcal{H}(t)$, then the equation can be expressed using the transformed system $G\zeta(t) = \psi(t)$, where $-\begin{bmatrix} c_f\left(L+G\right) & \mathbf{0}_{m\times(n-m)} \\ \mathbf{0}_{(n-m)\times m} & \mathbf{O}_{n-m} \end{bmatrix} - \mathcal{M}^P \mathcal{L}(\theta(t))$ is represented as $\mathcal{Q}(t) \in \mathbb{R}^{n\times n}$, $\begin{bmatrix} -c_f \tilde{\mathcal{L}} \odot \Theta \\ 0_{(n-m)\times m} \end{bmatrix}$ is represented as $\mathcal{D} \in \mathbb{R}^{n\times m}$, and $\begin{bmatrix} -c_f \left(\tilde{\mathcal{L}} \odot \Theta + \Lambda \odot \Xi\right) & \mathbf{0}_{m\times(n-m)} \end{bmatrix}$ is represented as $\mathcal{C} \in \mathbb{R}^{m\times n}$.

Then we obtain:

$$h(\zeta) = \underbrace{\begin{bmatrix} \mathcal{Q}(t) & \mathcal{D} \\ \mathcal{C} & -c_f\mathcal{L} \odot \Theta \end{bmatrix}}_{\mathcal{H}(t)} \zeta(t) + \begin{bmatrix} \mathbf{0}_{m\times(n-m)} \\ \operatorname{diag}\left(-\mathbf{1}_{n-m}^{\top}\right) \\ \mathbf{0}_{m\times(n-m)} \end{bmatrix} \dot{P}_L(t). \tag{3.11}$$

Thus, the state variables $\psi(t)$ of the system $\dot{\zeta}(t) = F(t)\zeta(t) + G\mathcal{Z}P_r(t)$ should satisfy Φ when belonging to the set Φ, where the matrix F satisfies $G\mathcal{H}(t) = F(t)G$. since $rank(G) = m$,

we have the Moore-Penrose $G^{\dagger} = G^T\left(GG^T\right)^{-1}$, So we get $F(t) = G\mathcal{H}(t)G^{\dagger}$, where, according to Problem 1, if the following condition holds:

$$\begin{aligned} &\max\left\{\mathfrak{T}[F(t)](\bar{\eta}+d)\mathbf{1}_m + \mathfrak{U}[F(t)](\bar{\eta}-d)\mathbf{1}_m + |G\mathcal{Z}|\bar{\alpha},\right. \\ &\left.\mathfrak{U}[F(t)](\bar{\eta}+d)\mathbf{1}_m + \mathfrak{T}[F(t)](\bar{\eta}-d)\mathbf{1}_m + |G\mathcal{Z}|\bar{\alpha}\right\} \preceq 0_n \end{aligned} \tag{3.12}$$

then constraint (2.9) is satisfied. Further calculation of the matrix $F(t) = \frac{1}{2}\left(\mathcal{Q}_{11}(t) - \mathcal{D}_{11} - \mathcal{C}_{11} - c_f L\right)$, where $F(t) = -\frac{1}{2}\mathcal{L}_{11}(t)$ represents the upper-left block, left-upper block, and left side of the matrix $F(t) = -\frac{1}{2}\mathcal{L}_{11}(t)$. Therefore, we have $F(t) = -\frac{1}{2}\mathcal{L}_{11}(t)$. Since the matrix $\mathcal{L}_{11}(t)$ is strictly diagonally dominant, the above condition can be easily simplified to:

$$\mathfrak{T}[F(t)](\overline{\eta}-d)1_m + |G\mathcal{Z}|\bar{\alpha} \preceq 0_n \tag{3.13}$$

Note that condition $G\mathcal{Z} = \mathbf{0}_{m\times(n-m)}$ (3.13) is always satisfied. Therefore, the system will always meet the power flow constraints in subsequent operating states, provided that the initial conditions satisfy constraint (2.9). Thus, the proof is complete. It can be demonstrated that the control strategy designed above ensures real-time satisfaction of the power flow constraints while maintaining completely distributed information acquisition, guaranteeing the existence of synchronized solutions.

Next, a cooperative control algorithm will be designed to synchronize the voltage magnitudes of all DG to the reference voltage v_{ref}. Based on the analysis in the first part, the voltage magnitudes of all DG are equivalent to directly synchronizing to the output voltage v_{odi}. The secondary voltage control involves selecting appropriate inputs V_{ni} to adapt to the previously proposed droop characteristics.

For the DG nonlinear system, it is important to note that the dynamics of the voltage-current controller are much faster than the dynamics of the power controller. Therefore, when considering only secondary control, the fast dynamic response of the voltage-current controller is ignored, and the droop equations can be written as:

$$\begin{cases} v_{\text{odi}} = V_{ni} - n_{Qi}Q_i \\ v_{\text{oqi}} = 0 \end{cases}. \tag{3.14}$$

By differentiating the above equation, we obtain:

$$\dot{v}_{odi} = \dot{V}_{ni} - n_{Qi}\dot{Q}_i \equiv u_{vi}. \tag{3.15}$$

Here, u_{vi} is an auxiliary control variable. In this dynamic system, the control input V_{ni} is obtained by calculating u_{vi}. Therefore, the secondary voltage control

problem of a microgrid containing N DGs is transformed into the tracking synchronization problem of a first-order linear multi-agent system. To achieve synchronization of v_{odi}, it is assumed that each DG communicates through a predefined directed communication graph G. The auxiliary control variable u_{vi} is selected based on its own information and the information from the neighbors in the directed graph, and is specifically described as:

$$\begin{aligned} u_{vi} &= -c_v e_{vi} - e_{zi}; \\ e_{vi} &= \sum_{j \in N_i} a_{ij} \left(v_{odi} - v_{odj} \right) + g_i \left(v_{odi} - v_{ref} \right). \end{aligned} \tag{3.16}$$

The control gain c_v and e_{vi} represent the local neighbor error, and $g_i \geq 0$ denotes the weight of the edge connecting the i-th DG to the reference. The elements of the adjacency matrix A can be expressed by a_{ij}. Any changes in the communication network will directly affect the matrix A, so when the communication topology changes, the coefficients a_{ij} must also change accordingly. The global neighbor error vector can be written as:

$$e = (L + G) \bullet (v_{od} - v_{ref}) \equiv (L + G)\delta. \tag{3.17}$$

The global variables are defined as:

$$\begin{aligned} v_{od} &= \left[\begin{array}{cccc} v_{od1} & v_{od2} & \ldots & v_{odN} \end{array} \right]^T, \\ e &= \left[\begin{array}{cccc} e_{v1} & e_{v2} & \ldots & e_{vN} \end{array} \right]^T, v_{ref} = 1_N \otimes v_{ref}. \end{aligned}$$

where 1_N is a unit vector of length N, and $\otimes$ represents the Kronecker product. $G \in \Re^{N \times N}$ is a diagonal matrix with diagonal elements equal to g_i, and δ is the global mismatch vector. The proof of system stability is the same as discussed above and will not be elaborated here.

The block diagram of secondary voltage control based on distributed cooperative control is shown in Figure 2. The control in is written as:

$$\begin{aligned} V_{ni} &= \int \left(u_{vi} + n_{Qi} \dot{Q}_i \right) dt, \\ \dot{Q} &= -\omega_c Q_i + \omega_c \left(v_{oqi} i_{odi} - v_{odi} i_{oqi} \right) = H_i \left(x_i \right) \end{aligned} \tag{3.18}$$

where ω_c is the cutoff frequency of the low-pass filter.

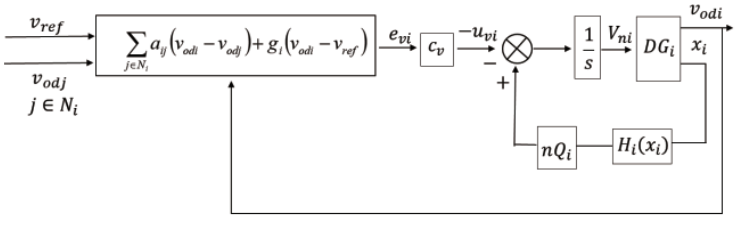

FIGURE 2. Block Diagram of Distributed Cooperative Secondary Voltage Control

The controller parameters in this paper are designed to ensure frequency and voltage synchronization among distributed generators (DGs) while satisfying power flow constraints. Key considerations include:

Auxiliary Control Variable: Set based on adjacent information among DGs to ensure neighbor error convergence in the communication graph. The variable is typically determined by frequency differences between neighboring DGs and the global neighbor error vector. A sufficiently sensitive gain coefficient is essential for rapid error response.

Weight Parameters in Communication Topology: Representing the connection strength between DGs, these weights should align with the physical connections and ensure stability during frequency synchronization. Real-time adjustments are required if the communication topology changes.

Voltage Control Gain Coefficient: Chosen based on neighbor information to synchronize voltage amplitude. This coefficient determines the system's response speed to voltage errors and should adapt to dynamic error variations.

Power Flow Allocation Constraint: Control parameters must ensure proportional power flow allocation during voltage and frequency control, maintaining consistency in power output ratios among DGs, as specified in the power flow constraint (Equation 2.9).

Remark. The main design parameters in the proposed control strategy, particularly those related to power synchronization and frequency control, include the control gains, adjacency matrix elements, and synchronization parameters from the equations. These parameters significantly impact the system's stability, convergence speed, and overshoot.

1. Control Gains and Adjacency Matrix Elements ($\hat{a}_{1j}, \vartheta_{ij}, a_{ij}$):

In the equation, $e_{pi} = \sum_{j\in N_i} \hat{a}_{1j} \cos(\theta_i - \theta_j)(m_{Pi}P_i - m_{Pj}P_j)$.

$\hat{a}_{1j}$ represents the weights for communication between DGs. These weights control how quickly and effectively each distributed generator (DG) responds to power mismatches with its neighbors. Higher values of $\hat{a}_{1j}$ can accelerate synchronization between DGs but can lead to overshooting if not properly tuned, particularly when $\cos(\theta_i - \theta_j)$ introduces oscillatory behavior.

Similarly, the parameter ϑ_{ij} in the update rule for $\hat{a}_{1j}$:

$$\dot{\hat{a}}_{1j} = \vartheta_{ij} a_{ij} \omega_i (\cos(\theta_i - \theta_j))(m_{Pi}P_i - m_{Pj}P_j),$$

influences the rate of adaptation of the communication weights. Increasing ϑ_{ij} improves the system's adaptability to power flow changes but may cause instability if the weights change too rapidly in response to high-frequency disturbances or noise.

2. Frequency Droop Coefficients (m_{Pi}, m_{Pj}):

The terms m_{Pi} and m_{Pj} represent the frequency droop coefficients of DGs i and j, respectively. These coefficients determine the degree to which the active power output P_i is adjusted in response to frequency deviations. A higher value of m_{Pi} makes DG i more responsive to power imbalances, improving synchronization speed. However, excessively high droop coefficients may cause instability due to over-compensation, leading to oscillations in frequency and power outputs.

4. Simulation verification

To verify the effectiveness of the proposed control strategy, a 4-DG microgrid system was constructed in MATLAB/Simulink, and simulation experiments were conducted using the RTLAB real-time simulator. Figure 3 depicts the basic architecture of the 4-DG system, which includes several local loads. The DG units are interconnected via RL-type lines, and the relevant key parameters are listed in Table 1. The corresponding network topology is also shown in Figure 3.

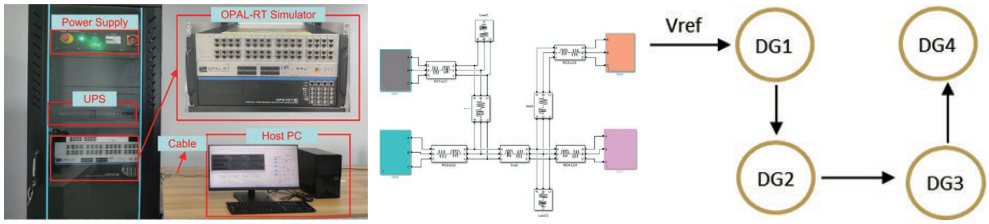

Figure 3. Physical and Network Communication Topology of Microgrids

Table 1. AC Microgrid System Parameters

	DG1&2		DG3&4	
DGs	mP	9.4e-5	mP	1.24e-4
	nQ	1.3e-4	nQ	1.5e-3
	Rc	0.03Ω	Rc	0.03Ω
	Lc	0.35mH	Lc	0.35mH
	Kpv	10	Kpv	10
	Kiv	100	Kiv	100
	Kpc	10	Kpc	10
	Kic	100	Kic	100
	Line 1	Line 2	Line 3	
R	0.23Ω	R	0.35Ω	R 0.23Ω
L	0.318mH	L	1.847mH	L 0.318mH
	$Load_1$		$Load_2$	
P	20kW		10kW	
Q	10kva		10kva	

Assume that the communication between each DG (Distributed Generator) follows the pattern shown in Figure 3, where the communication connections are chosen based on the geographical locations of the DGs. Therefore, the adjacent matrix of the directed graph (representing the communication network between the DGs) can be expressed as:

$$A = \begin{bmatrix} 0 & 0 & 0 & 0 \\ 1 & 0 & 0 & 0 \\ 0 & 1 & 0 & 0 \\ 0 & 0 & 1 & 0 \end{bmatrix}.$$

Only DG1 receives the reference signal from the leader, so at this point g_1; the choice of control gains c_v, c_ω, and c_p will affect the response speed of the controller.

This section of the study focuses on the following five aspects:

1. Comparison between primary and secondary control.
2. Load variations.
3. Plug-and-play performance of DGs.
4. Changes in communication topology.
5. Communication delays and data packet loss.

4.1. **Comparison between Primary and Secondary Control.** Before t=2s, the system was operated solely by the primary controller, and the secondary controller is not engaged. At time t=2s, the secondary controller is activated. From Figure 4, it can be observed that before time t=2s, the output voltages of each DG are not consistent. After t=2s, under the action of the secondary controller, the voltages of all DGs converge to 380V. From Figure 5, before time t=2s, the output frequencies of each DG have not reached $314rad/s$. After $314rad/s$, with the influence of the secondary controller, the frequencies of all DGs converge to $314rad/s$.

FIGURE 4. Output Voltage Waveforms of Each Distributed Generator (DG)

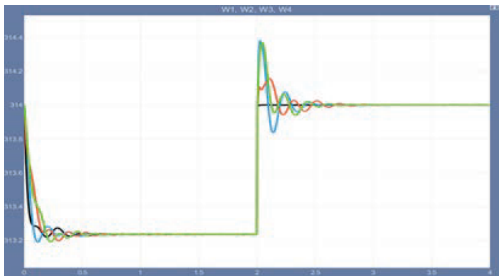

FIGURE 5. Output Frequency Waveforms of Each Distributed Generator (DG)

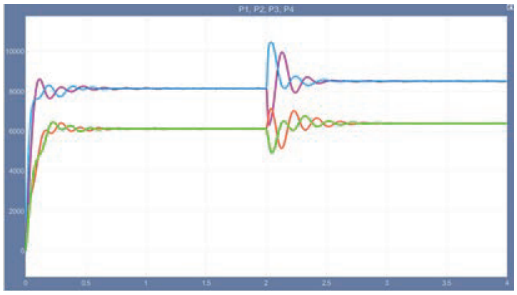

FIGURE 6. Output Active Power Waveforms of Each Distributed Generator (DG)

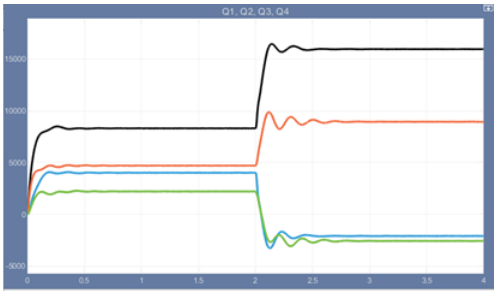

FIGURE 7. Output Reactive Power Waveforms of Each Distributed Generator (DG)

The active and reactive power outputs are allocated according to their respective internal droop characteristics. The output waveforms are shown in Figures 4 and 5. The results indicate that after adding the secondary control, the control performance becomes more reliable, and the tracking performance improves significantly. The curves of active and reactive power outputs are illustrated in Figures 6 and 7.

4.2. **Performance Analysis of Load Variations.** At time t=0s, the secondary controller is engaged. When t=0 arrives, the system experiences an increase of $P = 8kw$, $Q = 5kVA$ in load. From the simulation results, it can be observed that at the time t=0s, both the output voltage and frequency show fluctuations due to the sudden increase in load, which causes a decrease in frequency and an increase in voltage. However, the system quickly returns to the set values. Figures 8 and 9 show the output voltage waveforms and output frequency waveforms of each DG, respectively.

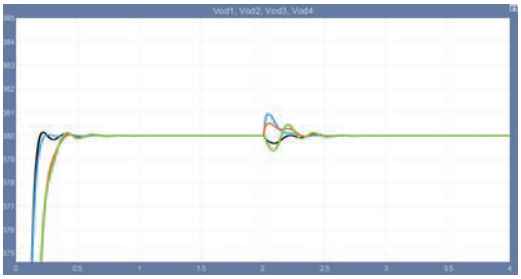

FIGURE 8. Output Voltage Waveforms of Each Distributed Generator (DG)

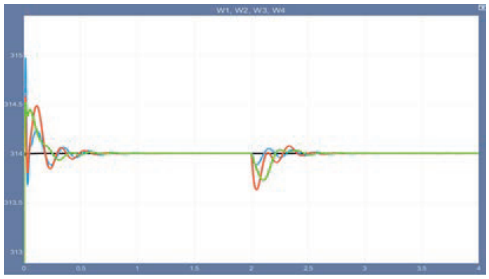

FIGURE 9. Output Frequency Waveforms of Each Distributed Generator (DG)

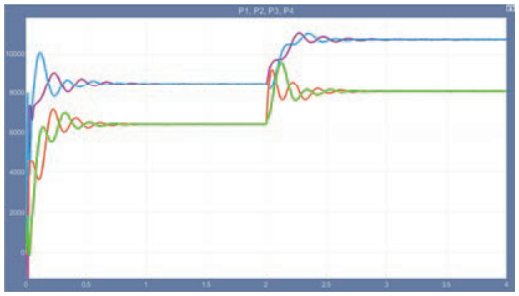

FIGURE 10. Output Active Power Waveforms of Each Distributed Generator (DG)

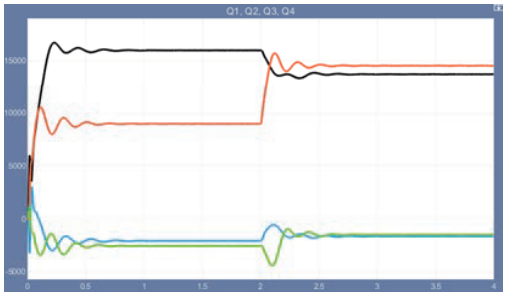

FIGURE 11. Output Reactive Power Waveforms of Each Distributed Generator (DG)

From Figures 10 and 11, with the increase in load, the output power also increases proportionally, without affecting the stability of the entire system. This indicates that the controller can track well and respond quickly.

4.3. **Plug-and-Play Performance Analysis of DGs.** At time t=0, the secondary controller is engaged, and DG1, DG3, and DG4 are connected to the system. At time t=2s, DG4 is removed from the system. At time t=0, DG2 is added to the system. From the simulation results, it can be observed that before time t=2s, under the action of the secondary controller, each DG connected to the microgrid system is able to converge to the set values and maintain stability.

At the time t=0s, when DG4 is removed from the system, the reduction in system output causes a temporary decrease in frequency and an increase in output voltage. The remaining DGs increase their output power. Subsequently, the system gradually returns to the set values.

At times of t=0s, when the number of DGs in the system increases, the load-carrying capacity improves. During this time, there is a brief increase in frequency and a decrease in output voltage. However, under the influence of the secondary controller, the system gradually returns to reference values. The entire switching process demonstrates that the proposed control algorithm responds quickly to the addition and removal of DGs without affecting the stability of the system. The specific simulation results are shown in Figures 12, 13, 14, and 15.

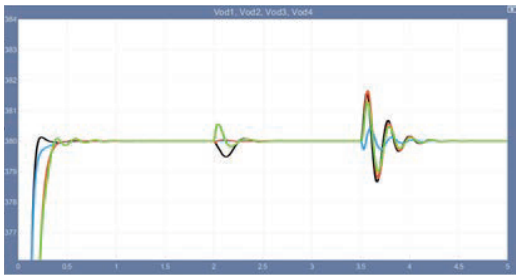

FIGURE 12. Voltage Waveforms of Each Distributed Generator

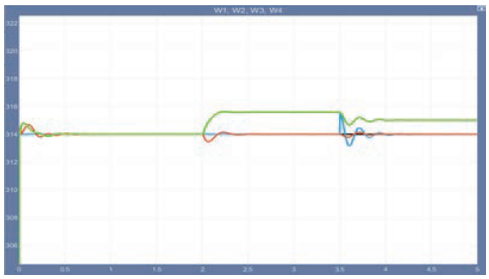

FIGURE 13. Frequency Waveforms of Each Distributed Generator

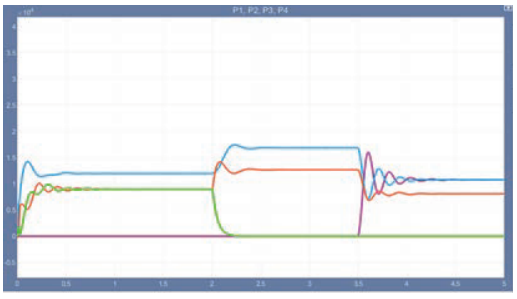

FIGURE 14. Active Power Waveforms of Each Distributed Generator

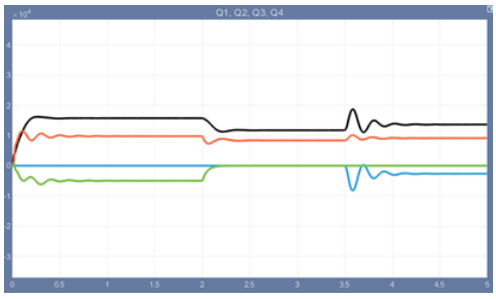

FIGURE 15. Reactive Power Waveforms of Each Distributed Generator

4.4. **Performance Analysis of Communication Topology Changes.** To verify the reliability of the control algorithm, it is important to assess whether changes in communication topology affect the stability of the system. At time t=1.5s, the system communicates between DGs using communication topology t=1.5s Between times t=1.5s and t=3.5s, the system switches to communication topology ② for communication. After time t=3.5s, communication topology ③ is used for DG communication.

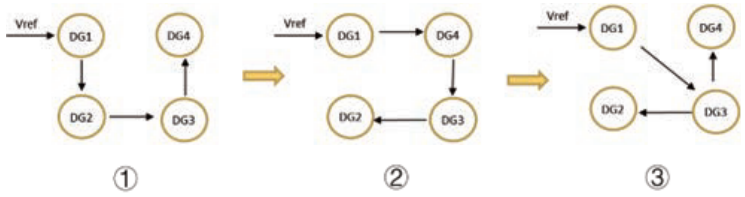

FIGURE 16. Communication Topology Changes.

Simulation results indicate that at each moment of communication topology switching, the system's voltage and frequency remain stable, demonstrating the strong robustness of the controller. The specific results are shown in Figures 17-20.

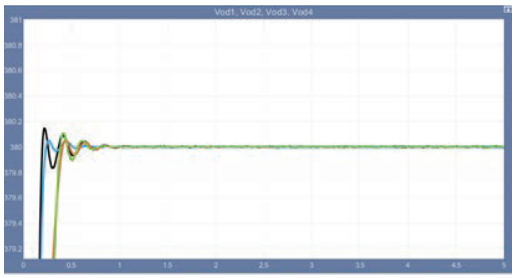

FIGURE 17. Voltage Waveforms of Each Distributed Generator (DG)

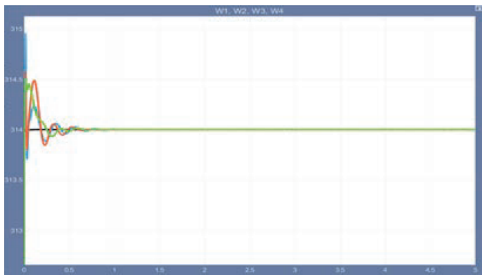

FIGURE 18. Frequency Waveforms of Each Distributed Generator (DG)

4.5. **Comparison with Fractional-Order Controllers and Observer Methods.** To validate the effectiveness of the proposed adaptive control algorithm in meeting power flow constraints, a Monte Carlo simulation was conducted. The simulation evaluated the system's performance under varying conditions, including random load changes, generation fluctuations, and line impedance variations. Each iteration of the simulation assessed the ability of the control algorithm to maintain system stability within predefined power flow limits. The results were compared with traditional PID and robust control methods.

Simulation Conditions:

Number of Iterations: 1000 Random Load Changes: ±30% of nominal load

External Disturbances: Random load changes and line failures

Control Algorithms: Adaptive Control Proposed in This Paper, PID Control, Robust Control.

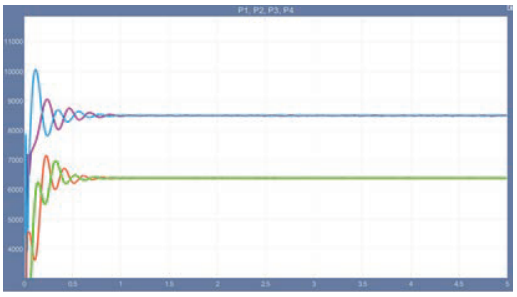

FIGURE 19. Active Power Waveforms of Each Distributed Generator (DG)

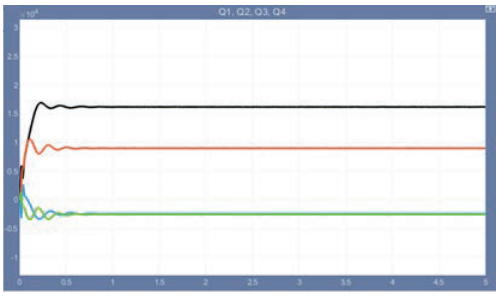

FIGURE 20. Reactive Power Waveforms of Each Distributed Generator (DG)

The results of the Monte Carlo simulation indicate that the proposed adaptive control algorithm maintains a 0% probability of losing stability under power flow constraints. In contrast, the PID control method exhibited a higher probability of instability at 18%, and the robust control method showed a 10% probability of losing stability. This demonstrates the exceptional reliability of the adaptive control algorithm in ensuring system stability under varying conditions.

5. Conclusion

In this study, an adaptive distributed control algorithm is proposed for voltage-frequency synchronization and active power allocation regulation in microgrids. Through in-depth analysis, a new adaptive distributed control algorithm is proposed to achieve fast voltage-frequency synchronization, adaptive allocation of active power, and adaptive allocation of active power.

References

[1] F. R. Albogamy, M. Zakria, T. A. Khan, S. Murawwat, G. Hafeez and I. Khan, *An optimal adaptive control strategy for energy balancing in smart microgrid using dynamic pricing*, IEEE Access, **10** (2022), 37396–37411.

[2] H. H. Ali, A. M. Kassem and M. Al-Dhaifallah, *Multi-verse optimizer for model predictive load frequency control of hybrid multi-interconnected plants comprising renewable energy*, IEEE Access **8** (2020), 114623–114642.

[3] S. Cordova, C. A. Canizares, A. Lorca and D. E. Olivares, *Frequen-cy-constrained energy management system for isolated microgrids*, IEEE Transactions on Smart Grid **13** (2022), 3394–3407.

[4] R. R. Deshmukh and M. S. Ballal, *Integrated control scheme for dynamic power management with improved voltage regulation in DC microgrid*, Journal of Power Electronics **20** (2020), 1550–1561.

[5] F. Dubuisson, M. Rezkallah, H. Ibrahim and M. Cherkaoui, *Real-time implementation of the predictive-based control with bacterial foraging optimization technique for power management in standalone microgrid application*, Energies **14** (2021), 1722–1737.

[6] S. Ferahtia, A. Djeroui, H. Rezk, A. Houari, S. Zeghlache and M. Machmoum, *Optimal control and implementation of energy management strategy for a DC microgrid*, Energy **238** (2022): 121777.

[7] N. Gao, B. Zhang, W. Wu, X. Liu and Y. Ma, *Finite control set model predictive control integrated with disturbance observer for battery energy storage power conversion system*, Journal of Power Electronics **21** (2021), 342–353.

[8] J.M. Guerrero, J.C. Vasquez, J. Matas, M. Castilla and L.G. Garcáa de Vicuña, *Hierarchical control of droop-controlled AC and DC microgrids-A general approach Toward Standardization*, IEEE Transactions on Industrial Electronics **58** (2011), 158–172.

[9] H. Han, X. Chen and Z. Liu, *A completely cooperative economic dispatching strategy considering capacity constraints*, IEEE Journal of Selected Topics in Circuits and Systems **11** (2021), 210–221.

[10] S. Li and X. Hou, *Research on power control technology of high proportion of photovoltaic energy connected to microgrid system*, Light Source and Illumination **09** (2024), 104–106.

[11] Y. Li, X. Liu, Y. Wu and W. Qian, *Improved droop control of hybrid AC/DC microgrid with optimal power sharing strategy*, Electric Power Systems Research **201** (2021): 107531.

[12] J. A. P. Lopes, C. L. Moreira and A. G. Madureira, *Defining control strategies for MicroGrids islanded operation*, IEEE Transactions on Power Systems, **21** (2006), 916–924.

[13] T.L. Nguyen, H.T. Nguyen, Y. Wang, O.A. Mohammed and E. Anagnostou, *Distributed secondary control in microgrids using synchronous condenser for voltage and frequency support*, Energies **15** (2022), 1–15.

[14] T. Pippia, J. Sijs and B. De Schutter, *A single-level rule-based model predictive control approach for energy management of grid-connected microgrids*, IEEE Transactions on Control Systems Technology **28** (2020), 2364–2376.

[15] D. Qin, R. Fu and M.Y. Wang, *Stability control method of microgrid based on adaptive droop coefficient*, Electrical Automation **46** (2024), 23–26+30.

[16] G. Rigatos, M. Abbaszadeh, F. Zouari, P. Siano, M. Al-Numay and G. Cuccurullo, *Flatness-based disturbance observer and control for a robotic mining excavator*, (2024), PREPRINT (Version 1) available at Research Square [https://doi.org/10.21203/rs.3.rs-4972304/v1]

[17] G. Rigatos, K. Busawon, M. Abbaszadeh, J. Pomares, Z. Gao and F. Zouari, *Flatness-based control in successive loops for dual-arm robotic manipulators*, in: 2024 IEEE Conference on Control Technology and Applications (CCTA), IEEE, 2024, pp. 793–798.

[18] J.W. Simpson-Porco, F. Dorfler and F. Bullo, *Synchronization and power sharing for droop-controlled inverters in islanded microgrids*, Automatica **49** (2013), 2603–2611.

[19] A. Taheri, Y. Zhang, X. Yan and C. Sun, *Adaptive droop control for dynamic power sharing in microgrids*, IEEE Transactions on Smart Grid **13** (2020), 26–36.

[20] L. L. Xiong, L. You and G. Han, *Unbalance and harmonic control of grid-structured converter based on uniform voltage-current droop*, Journal of Power Supply, **22** (2024), 1–16.

[21] S. A. Zaid, A. M. Kassem, A. M. Alatwi, H. Albalawi, H. AbdelMeguid and A. Elemary, *Optimal control of an autonomous microgrid integrated with super magnetic energy storage using an artificial bee colony algorithm*, Sustainability **15** (2023): 8827.

[22] P. Zhang, Y. Wang, Y. Wei and S. Li, *Secondary voltage control in distributed generation systems based on multi-agent systems*, IET Renewable Power Generation **15** (2021), 3856–3872.

[23] F. Zouari, A. Ibeas, A. Boulkroune and J. Cao, *Finite-time adaptive event-triggered output feedback intelligent control for noninteger order nonstrict feedback systems with asymmetric time-varying pseudo-state constraints and nonsmooth input nonlinearities*, Communications in Nonlinear Science and Numerical Simulation **136** (2024): 108036.

Manuscript received September 19, 2024
revised December 22, 2024

Z. Li
Digital Grid Research Institute, China Southern Power Grid, Guangzhou 510000, China; Guangdong Provincial Key Laboratory of Digital Grid Technology, China Southern Power Grid, Guangzhou 510000, China
E-mail address: zhuohuan12@csg.cn

D. Yang
Digital Grid Research Institute, China Southern Power Grid, Guangzhou 510000, China; Guangdong Provincial Key Laboratory of Digital Grid Technology, China Southern Power Grid, Guangzhou 510000, China
E-mail address: Jerry19860102@yeah.net

C. Zhou
Digital Grid Research Institute, China Southern Power Grid, Guangzhou 510000, China; Guangdong Provincial Key Laboratory of Digital Grid Technology, China Southern Power Grid, Guangzhou 510000, China
E-mail address: cczhou@csg.cn

K. Cheng
Digital Grid Research Institute, China Southern Power Grid, Guangzhou 510000, China; Guangdong Provincial Key Laboratory of Digital Grid Technology, China Southern Power Grid, Guangzhou 510000, China
E-mail address: kcheng128@163.com

Y. Yu
Digital Grid Research Institute, China Southern Power Grid, Guangzhou 510000, China; Guangdong Provincial Key Laboratory of Digital Grid Technology, China Southern Power Grid, Guangzhou 510000, China
E-mail address: yangy368@yeah.net

S. Yang
Digital Grid Research Institute, China Southern Power Grid, Guangzhou 510000, China; Guangdong Provincial Key Laboratory of Digital Grid Technology, China Southern Power Grid, Guangzhou 510000, China
E-mail address: sryang@csg.cn